Microsyst Technol (2012) 18:1343–1351
DOI 10.1007/s00542-012-1540-y

TECHNICAL PAPER

Friction effect on ball positioning of an automatic balancer in optical disk drives

T. C. Chan · C. K. Sung · Paul C. P. Chao

Received: 25 July 2011 / Accepted: 22 May 2012 / Published online: 15 June 2012
© Springer-Verlag 2012

Abstract This study was aimed at evaluating the perfect balancing position of an automatic ball balancer installed in optical disk drives taking into consideration the effects of the rolling friction, speed ratio, and scaling parameter on ball positioning. A mathematical model that is employed to derive the dynamic equations of the ABB system was constructed. Stability of the steady-state solutions was then analyzed. A numerical simulation and an experimental study were conducted to verify the mathematical model. The simulation and experimental results were in good agreement.

List of symbols

G_R	Center of gravity (C.G.) of the equivalent rotor
G_S	Center of gravity of the equivalent stator
M_R	Mass of the equivalent rotor
M_S	Mass of the equivalent stator
O_B	Center of a ball
O_S	Rotational center of the rotor
O_R	Origin of the inertial coordinate
O_r	Center of the circular race of the balancer
ρ	Race eccentricity
e	Imbalanced eccentricity
β	Lead angle for imbalance
ϕ_i	Angle of ball's positions
Bi	Number of balls
m	Ball mass
r	Ball radius
K_X	Stiffness in the X direction
K_Y	Stiffness in the Y direction
C_x	Damping in the X direction
C_y	Damping in the Y direction
p	Speed ratio ω/ω_n
ε	Scaling parameter $\sqrt{m/M}$
ω_n	Natural frequency of the suspension
τ	Normalized time scale
R	Race radius
α_1	Adhesive coefficient
α_0	Rolling friction coefficient of the ball balancer
θ	Rotating angle of the disk

T. C. Chan · C. K. Sung (✉)
Department of Power Mechanical Engineering,
National Tsing Hua University, Hsinchu 30013,
Taiwan, ROC
e-mail: cksung@pme.nthu.edu.tw

T. C. Chan
e-mail: d9533830@oz.nthu.edu.tw

T. C. Chan
Precision Machinery Research and Development Center,
Taichung 40768, Taiwan, ROC

P. C. P. Chao
Department of Electrical Engineering, National Chiao
Tung University, Hsinchu 30013, Taiwan, ROC
e-mail: pchao@mail.nctu.edu.tw

P. C. P. Chao
Institute of Imaging and Biomedical Photonics,
National Chiao Tung University, Tainan 711, Taiwan, ROC

1 Introduction

Imbalances are the common causes of vibrations in high-speed optical disk drives. The perfect balancing position of an automatic ball balancer (ABB) can almost completely eliminate radial vibrations via the phenomenon of counterbalancing. A recent challenge for ABBs used in high speed optical disk drives is the inconsistency of the balls' positioning due to the rolling friction of the balancing balls.

Quangang et al. (2004) and Chao et al. (2005) investigated the influence of friction in an ABB. Van De Wouw et al. (2005) evaluated the performance of an ABB with dry friction. Rajalingham and Bhat (2006) incorporated contact friction of the balancing balls in a model. Chao et al. (2007) presented a non-planar dynamic model and an experimental validation of a spindle-disk system equipped with an ABB. Lu et al. (2008) proposed general guidelines on the stability of the equilibrium positions of an ABB. DeSmidt (2009) developed a new analysis method for calculating the dynamics and stability of an imbalanced flexible shaft equipped with an ABB. Liu and Ishida (2009) presented the vibration suppression method utilizing the discontinuous spring characteristics together with an ABB. Chan et al. (2011) investigated the effects of the non-linear suspensions of an ABB installed in a rotor system on ball positioning. Cheng et al. (2008) and Lim et al. (2011) designed an optical disk drive using speed-dependent vibration absorbers in specific frequency ranges. Rodrigues et al. (2011) conducted an experimental investigation of a single-plane with a two-ball ABB. From these related studies, it is obvious that correct ball positioning is the most important requirement for an ABB. Therefore, The ABB needs to be re-evaluated for design guidelines with a thorough exploration of parameters such as the rolling friction, scaling parameter, and speed ratio.

2 Mathematical model

The photograph of an ABB in an optical disk drive is shown in Fig. 1. The physical system can be simplified. This is shown schematically in Fig. 2; without a loss of generality, the simplified system, is considered to contain a pair of balls with mass m and radius r.

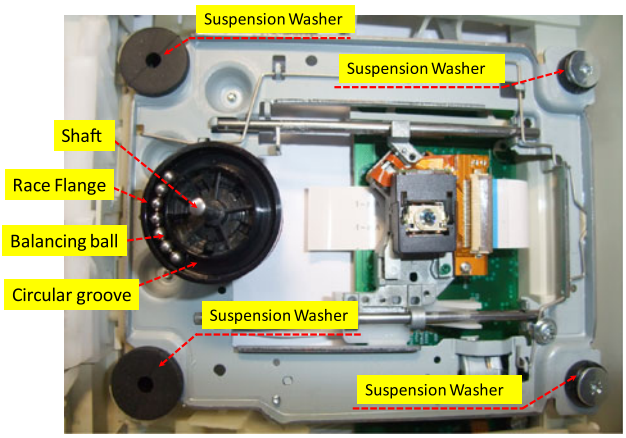

Fig. 1 Photograph of an automatic ball balancer in an optical disk drive

The equations of motion of the optical disk drive are derived below, where $M = M_R + M_S + nm$. The equations of motion of the equivalent rotor for multiple balls can be derived by balancing inertial forces of the rotor, interactive forces by balls, and resistant forces by suspension, which are listed as the following:

$$\begin{aligned}
M\ddot{X} + C_x\dot{X} + K_X X &= M_R[\rho\ddot{\theta}\sin\theta + \rho\dot{\theta}^2\cos\theta + e\ddot{\theta}\sin(\theta+\beta) \\
&\quad + e\dot{\theta}^2\cos(\theta+\beta)] + m\sum_{i=1}^{n}[\rho\ddot{\theta}\sin\theta \\
&\quad + \rho\dot{\theta}^2\cos\theta + R(\ddot{\theta}+\ddot{\phi}_i)\sin(\theta+\phi_i) \\
&\quad + R(\dot{\theta}+\dot{\phi}_i)^2\cos(\theta+\phi_i)] \\
M\ddot{Y} + C_Y\dot{Y} + K_Y Y &= M_R[-\rho\ddot{\theta}\cos\theta + \rho\dot{\theta}^2\sin\theta - e\ddot{\theta}\cos(\theta \\
&\quad + \beta) + e\dot{\theta}^2\sin(\theta+\beta)] + m\sum_{i=1}^{n} \\
&\quad \times [-\rho\ddot{\theta}\cos\theta + \rho\dot{\theta}^2\sin\theta - R(\ddot{\theta}+\ddot{\phi}_i) \\
&\quad \times \cos(\theta+\phi_i) + R(\dot{\theta}+\dot{\phi}_i)^2\sin(\theta+\phi_i)] \\
\left(m+\frac{I}{r^2}\right)R(\ddot{\phi}_i+\ddot{\theta}) &= m[(\ddot{X} - \rho\ddot{\theta}\sin\theta - \rho\dot{\theta}^2\cos\theta)\sin(\phi_i+\theta) \\
&\quad - (\ddot{Y} + \rho\ddot{\theta}\cos\theta - \rho\dot{\theta}^2\sin\theta)\cos(\phi_i+\theta)] \\
&\quad - \alpha_1 R\dot{\phi} - \frac{M_f}{r}sign(\dot{\phi}_i) + \frac{(R+r)}{r^2}I\ddot{\theta} \\
&\quad i = 1,2,3,\ldots,n
\end{aligned} \tag{1}$$

where $M_f$is the moment of the rolling friction, which is mainly due to the rolling friction between the balancing ball and the outer flange of the race.

$$\begin{aligned}
M_f = \alpha_0 m[R(\dot{\theta}+\dot{\varphi}_i)^2 - (\ddot{X} - \rho\ddot{\theta}\sin\theta - \rho\dot{\theta}^2\cos\theta)\cos(\theta \\
+ \phi_i) - (\ddot{Y} + \rho\ddot{\theta}\cos\theta - \rho\dot{\theta}^2\sin\theta)\sin(\theta+\phi_i)]
\end{aligned} \tag{2}$$

3 Asymptotic analysis

By making some scaling assumptions and then employing asymptotic analysis techniques i.e., the multiple-scale analysis, we seek approximate solutions for the system in order to manipulate the equations of motion. Maintaining the mass of the balancing ball, m, at a value that is considerably smaller than the mass of the system, M, results in $\varepsilon = \sqrt{m/M}$, which is the scaling parameter. Using this defined parameter, the system parameters in Eq. (1) are rearranged to an amenable form for multiple-scale analysis.

$$\begin{aligned}
&\tau = \omega_n t, \varepsilon x = X/R, \varepsilon y = Y/R, \omega_n = \sqrt{K/M}, \varepsilon_2\lambda_1 \\
&= \rho/R, \varepsilon_3\lambda_2 = e/R, \mu = m/(m+I/r^2), \varepsilon\zeta = C/M\omega_n, \varepsilon\lambda \\
&= (r+R)I/mr^2R, \alpha = M_R/M, \varepsilon\zeta_0 = \alpha_0/r, \varepsilon\zeta_1 \\
&= \alpha_1/m\omega_n, \varepsilon_1 \approx \varepsilon, \varepsilon_2 \approx \varepsilon^2, \varepsilon_3 \approx \varepsilon^2,
\end{aligned}$$

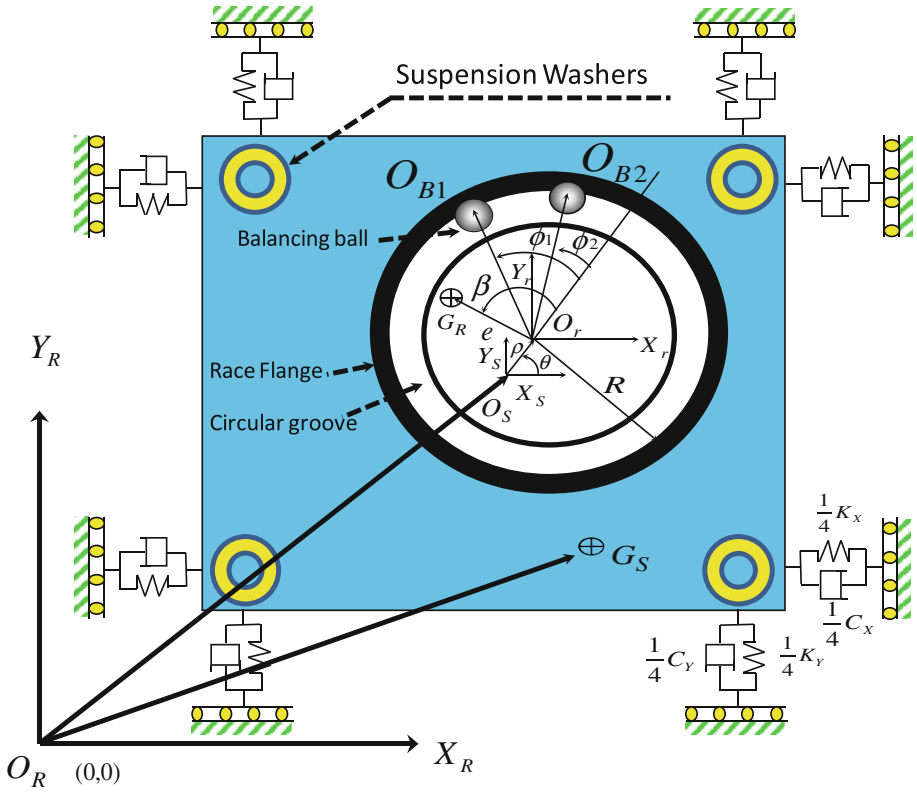

Fig. 2 Schematic representation of the ABB in an optical disk drive

where λ_1 and λ_2 are the nondimensionalized race and center of mass eccentricity, respectively. The system experiences weaker excitation and the response scaling $\varepsilon x = X/R$ and $\varepsilon y = Y/R$ of the system. Substituting the definition of ε and the scaling assumptions into the system, we obtain

$$\begin{aligned}
\ddot{x} + x &= \varepsilon\{ -\zeta\dot{x} + \alpha\{\lambda_1(\ddot{\theta}\sin\theta + \dot{\theta}^2\cos\theta) + \lambda_2[\ddot{\theta}\sin(\theta \\
&\quad + \beta) + \dot{\theta}^2\cos(\theta+\beta)]\} + \sum_{i=1}^{n}[\varepsilon^2\lambda_1(\ddot{\theta}\sin\theta \\
&\quad + \dot{\theta}^2\cos\theta) + (\ddot{\theta}+\ddot{\phi}_i)\sin(\theta+\phi_i) + (\dot{\theta}+\dot{\phi}_i)^2 \\
&\quad \times\cos(\theta+\phi_i)]\} \\
\ddot{y} + y &= \varepsilon\{ -\zeta\dot{y} + \alpha\{\lambda_1(-\ddot{\theta}\cos\theta + \dot{\theta}^2\sin\theta) \\
&\quad + \lambda_2[-\ddot{\theta}\cos(\theta+\beta) + \dot{\theta}^2\sin(\theta+\beta)]\} \\
&\quad + \sum_{i=1}^{n}[\varepsilon^2\lambda_1(-\ddot{\theta}\cos\theta + \dot{\theta}^2\sin\theta) - (\ddot{\theta} \\
&\quad + \ddot{\phi}_i)\cos(\theta+\phi_i) + (\dot{\theta}+\dot{\phi}_i)^2\sin(\theta+\phi_i)]\} \\
(\ddot{\phi}_i + \ddot{\theta}) &= \varepsilon\{\mu\{[\ddot{x} + \varepsilon\lambda_1(-\ddot{\theta}\sin\theta - \dot{\theta}^2\cos\theta)]\sin(\phi_i+\theta) \\
&\quad - [\ddot{y} + \varepsilon\lambda_1(\ddot{\theta}\cos\theta - \dot{\theta}^2\sin\theta)]\cos(\phi_i+\theta) \\
&\quad - \zeta_1\dot{\phi}_i - \zeta_0\{(\dot{\theta}+\dot{\phi}_i)^2 - [\varepsilon\ddot{x} + \varepsilon^2\lambda_1(-\ddot{\theta}\sin\theta \\
&\quad - \dot{\theta}^2\cos\theta)]\cos(\theta+\phi) - [\varepsilon\ddot{y} + \varepsilon^2\lambda_1(\ddot{\theta}\cos\theta \\
&\quad - \rho\dot{\theta}^2\sin\theta)]\sin(\theta+\phi)\}sign(\dot{\phi}_i) + \lambda\ddot{\theta}\}\}
\end{aligned} \tag{3}$$

From these equations, the steady-state solutions and the corresponding stability of the system are of interest. In the steady state, the rotor speed approaches a constant $\dot{\theta}$. For simplicity, this constant speed is denoted by $\omega = \dot{\theta}$. Then, $p = \omega/\omega_n$ is defined as the speed ratio, where ω_n is the natural frequency of the suspension system. Furthermore, a normalizing time scale $\tau = \omega_n t$ is introduced that renders $\ddot{\theta} = 0$, $\dot{\theta} = p$, and $\theta = p\tau$. To facilitate the ensuing asymptotic analysis, the square of the speed ratio p is represented by $p^2 = 1 + \varepsilon\sigma$, where σ describes the scaled deviation of p^2 from one. It is worth noting that the scaling assumption $p^2 = 1 + \varepsilon\sigma$ implies that the following analysis is valid only near the natural frequency of the system. The solutions show that because the system undergoes weak excitation, no sub-harmonic resonance is present. Therefore, the approximate solutions are expected to predict the dynamics of the system away from the primary resonance. We use the aforementioned definitions and assumptions to manipulate Eq. (3) into matrices. Next, the dynamic response can be acquired from a direct numerical simulation using MATLAB. In Eq. (3), the overdots and double overdots denote differentiation and double differentiation with respect to a new time scale τ, respectively. The application of the multiple-scale analysis is given by Eq. (3). Assume that

$$\begin{aligned} x(\tau;\varepsilon) &= x_0(T_0,T_1) + \varepsilon x_1(T_0,T_1) + O(\varepsilon^2) \\ y(\tau;\varepsilon) &= y_0(T_0,T_1) + \varepsilon y_1(T_0,T_1) + O(\varepsilon^2) \\ \phi_1(\tau;\varepsilon) &= \phi_{10}(T_0,T_1) + \varepsilon\phi_{11}(T_0,T_1) + O(\varepsilon^2) \\ \phi_2(\tau;\varepsilon) &= \phi_{20}(T_0,T_1) + \varepsilon\phi_{21}(T_0,T_1) + O(\varepsilon^2) \end{aligned} \tag{4}$$

where $T_0 = \tau$ is the fast time scale and $T_1 = \varepsilon\tau$ is the slow time scale. The introduction of T_0 and T_1 renders

$$\frac{d}{d\tau} = D_0 + \varepsilon D_1 + O(\varepsilon^2), \frac{d^2}{d\tau^2} = D_0^2 + 2\varepsilon D_0 D_1 + O(\varepsilon^2), \tag{5}$$

where $D_n = \frac{\partial}{\partial T_n}$ for $n = 0, 1$. Substituting assumptions (4) and transformations (5) into Eq. (3) and ignoring $O(\varepsilon^2)$ terms. We equate the coefficients accompanied by ε^1 and derive the dynamics of the order ε^1 as

$$\begin{aligned} D_0^2 x_1 + p^2 x_1 = e^{ipT_0}\Bigg[&-2pi\frac{\partial A_0}{\partial T_1} - \zeta pi A_0 \\ &+ \sigma A_0 + \frac{\alpha p^2\lambda_1}{2} + \frac{\alpha p^2\lambda_2 e^{i\beta}}{2} + \frac{(p+\psi_{10})^2 e^{i\phi_{10}}}{2} \\ &+ \frac{(p+\psi_{20})^2 e^{i\phi_{20}}}{2}\Bigg] + e^{-ipT_0}\Bigg[2pi\frac{\partial\overline{A_0}}{\partial T_1} \\ &+ \zeta pi\overline{A}_0 + \sigma\overline{A}_0 + \frac{\alpha p^2\lambda_1}{2} + \frac{\alpha p^2\lambda_2 e^{-i\beta}}{2} \\ &+ \frac{(p+\psi_{10})^2 e^{-i\phi_{10}}}{2} + \frac{(p+\psi_{20})^2 e^{-i\phi_{20}}}{2}\Bigg] \end{aligned}$$

$$\begin{aligned} D_0^2 y_1 + p^2 y_1 = e^{ipT_0}\Bigg[&-2pi\frac{\partial B_0}{\partial T_1} - \zeta pi B_0 + \sigma B_0 - \frac{i\alpha p^2\lambda_1}{2} \\ &- \frac{i\alpha p^2\lambda_2 e^{i\beta}}{2} - \frac{i(p+\psi_{10})^2 e^{i\phi_{10}}}{2} \\ &- \frac{i(p+\psi_{20})^2 e^{i\phi_{20}}}{2}\Bigg] + e^{-ipT_0}\Bigg[2pi\frac{\partial\overline{B}_0}{\partial T_1} \\ &+ \zeta pi\overline{B}_0 + \sigma\overline{B}_0 + \frac{i\alpha p^2\lambda_1}{2} + \frac{i\alpha p^2\lambda_2 e^{-i\beta}}{2} \\ &+ \frac{i(p+\psi_{10})^2 e^{-i\phi_{10}}}{2} + \frac{i(p+\psi_{20})^2 e^{-i\phi_{20}}}{2}\Bigg] \end{aligned}$$

$$\begin{aligned} D_0^2\phi_{11} = &e^{i(2pT_0+\phi_{10})}\left[\frac{\mu p^2(iA_0+B_0)}{2}\right] + e^{-i(2pT_0+\phi_{10})} \\ &\times\left[\frac{\mu p^2(-i\overline{A}_0+\overline{B}_0)}{2}\right] + \Bigg\{-2\frac{\partial\psi_{10}}{\partial T_1} \\ &+ e^{-i\varphi_{10}}\left[\frac{\mu p^2(-iA_0+B_0)}{2}\right] \\ &+ e^{i\phi_{10}}\left[\frac{\mu p^2(i\overline{A}_0+\overline{B}_0)}{2}\right] + \mu[-\zeta_1\psi_{10} \\ &- \zeta_0(p+\psi_{10})^2\mathrm{sgn}(\psi_{10})\Bigg]\Bigg\} \end{aligned}$$

$$\begin{aligned} D_0^2\phi_{21} = &e^{i(2pT_0+\phi_{20})}\left[\frac{\mu p^2(iA_0+B_0)}{2}\right] \\ &+ e^{-i(2pT_0+\phi_{20})}\left[\frac{\mu p^2(-i\overline{A}_0+\overline{B}_0)}{2}\right] \\ &+ \Bigg\{-2\frac{\partial\psi_{20}}{\partial T_1} + e^{-i\phi_{20}}\left[\frac{\mu p^2(-iA_0+B_0)}{2}\right] \\ &+ e^{i\phi_{20}}\left[\frac{\mu p^2(i\overline{A}_0+\overline{B}_0)}{2}\right] + \mu\Bigg[-\zeta_1\psi_{20} \\ &- \zeta_0(p+\psi_{20})^2\mathrm{sgn}(\psi_{20})\Bigg]\Bigg\} \end{aligned} \tag{6}$$

The solutions of Eq. (6) are x_1, y_1, ϕ_{11}, and ϕ_{21} and are expressed as follows:

$$\begin{aligned} x_1 = &A_1(T_1)e^{ipT_0} + \overline{A}_1(T_1)e^{-ipT_0} + \frac{1}{2ip}\Bigg[A_{11}(T_1)T_0 e^{ipT_0} \\ &- \overline{A}_{11}(T_1)T_0 e^{-ipT_0}\Bigg] \\ y_1 = &B_1(T_1)e^{ipT_0} + \overline{B}_1(T_1)e^{-ipT_0} + \frac{1}{2ip}\Bigg[B_{11}(T_1)T_0 e^{ipT_0} \\ &- \overline{B}_{11}(T_1)T_0 e^{-ipT_0}\Bigg] \\ \phi_{11} = &\frac{e^{i(2pT_0+\phi_{10})}}{-(2p+\psi_{10})^2}\left[\frac{\mu p^2(iA_0+B_0)}{2}\right] + \frac{e^{-i(2pT_0+\phi_{10})}}{-(2p+\psi_{10})^2} \\ &\times\left[\frac{\mu p^2(-i\overline{A}_0+\overline{B}_0)}{2}\right] + \Bigg\{-2\frac{\partial\psi_{10}}{\partial T_1} \\ &+ e^{-i\phi_{10}}\left[\frac{\mu p^2(-iA_0+B_0)}{2}\right] + e^{i\phi_{10}}\left[\frac{\mu p^2(i\overline{A}_0+\overline{B}_0)}{2}\right] \\ &+ \mu\Bigg[-\zeta_1\psi_{10} - \zeta_0(p+\psi_{10})^2\mathrm{sgn}(\psi_{10})\Bigg]\Bigg\}\frac{T_0^2}{2} \\ \phi_{21} = &\frac{e^{i(2pT_0+\phi_{20})}}{-(2p+\psi_{20})^2}\left[\frac{\mu p^2(iA_0+B_0)}{2}\right] + \frac{e^{-i(2pT_0+\phi_{20})}}{-(2p+\psi_{20})^2} \\ &\times\left[\frac{\mu p^2(-i\overline{A}_0+\overline{B}_0)}{2}\right] + \Bigg\{-2\frac{\partial\psi_{20}}{\partial T_1} \\ &+ e^{-i\phi_{20}}\left[\frac{\mu p^2(-iA_0+B_0)}{2}\right] + e^{i\phi_{20}}\left[\frac{\mu p^2(i\overline{A}_0+\overline{B}_0)}{2}\right] \\ &+ \mu\Bigg[-\zeta_1\psi_{20} - \zeta_0(p+\psi_{20})^2\mathrm{sgn}(\psi_{20})\Bigg]\Bigg\}\frac{T_0^2}{2} \end{aligned} \tag{7}$$

Because T_0 is the fast time scale and T_1 is the slow time scale, the coefficients of T_0 andT_0^2 are zero. If they are not

equal to zero, then x_1, y_1, ϕ_{11}, and ϕ_{21} approach infinity. Next, we obtain

$$A_{11} = \left[-2pi\frac{\partial A_0}{\partial T_1} - \zeta pi A_0 + \sigma A_0 + \frac{\alpha p^2 \lambda_1}{2} + \frac{\alpha p^2 \lambda_2 e^{i\beta}}{2} + \frac{(p+\psi_{10})^2 e^{i\phi_{10}}}{2} + \frac{(p+\psi_{20})^2 e^{i\phi_{20}}}{2} \right] = 0$$

$$B_{11} = \left[-2pi\frac{\partial B_0}{\partial T_1} - \zeta pi B_0 + \sigma B_0 - \frac{i\alpha p^2 \lambda_1}{2} - \frac{i\alpha p^2 \lambda_2 e^{i\beta}}{2} - \frac{i(p+\psi_{10})^2 e^{i\phi_{10}}}{2} - \frac{i(p+\psi_{20})^2 e^{i\phi_{20}}}{2} \right] = 0$$

$$\left\{ -2\frac{\partial \psi_{10}}{\partial T_1} + e^{-i\phi_{10}} \left[\frac{\mu p^2 (-iA_0 + B_0)}{2} \right] + e^{i\phi_{10}} \left[\frac{\mu p^2 (i\overline{A}_0 + \overline{B}_0)}{2} \right] + \mu \left[-\zeta_1 \psi_{10} - \zeta_0 (p + \psi_{10})^2 \mathrm{sgn}(\psi_{10}) \right] \right\} = 0$$

$$\left\{ -2\frac{\partial \psi_{20}}{\partial T_1} + e^{-i\phi_{20}} \left[\frac{\mu p^2 (-iA_0 + B_0)}{2} \right] + e^{i\phi_{20}} \left[\frac{\mu p^2 (i\overline{A}_0 + \overline{B}_0)}{2} \right] + \mu \left[-\zeta_1 \psi_{20} - \zeta_0 (p + \psi_{20})^2 \mathrm{sgn}(\psi_{20}) \right] \right\} = 0 \quad (8)$$

The exponential forms in Eq. (6) are used to calculate the trigonometric functions for simplifying the ensuing computations. The removal of the secular terms from Eq. (6) leads to four conditions. Incorporating formulations for $A_0, \bar{A}_0, B_0$, and $\bar{B}_0$ in real-imaginary forms

$$A_0 = a(T_1) + ib(T_1), \overline{A}_0 = a(T_1) - ib(T_1),$$
$$B_0 = c(T_1) + id(T_1), \overline{B}_0 = c(T_1) - id(T_1), \quad (9)$$

into the four secular term removal conditions leads to the following solutions.

$$\frac{\partial a}{\partial \tau} = \frac{\varepsilon}{2p} \left[-\zeta pa + \sigma b + \frac{\alpha p^2 \lambda_2 \sin\beta}{2} + \frac{(p+\psi_{10})^2 \sin\phi_{10}}{2} + \frac{(p+\psi_{20})^2 \sin\phi_{20}}{2} \right]$$

$$\frac{\partial b}{\partial \tau} = \frac{-\varepsilon}{2p} \left[\zeta pb + \sigma a + \frac{\alpha p^2 \lambda_1}{2} + \frac{\alpha p^2 \lambda_2 \cos\beta}{2} + \frac{(p+\psi_{10})^2 \cos\phi_{10}}{2} + \frac{(p+\psi_{20})^2 \cos\phi_{20}}{2} \right]$$

$$\frac{\partial c}{\partial \tau} = \frac{\varepsilon}{2p} \left[-\zeta pc + \sigma d - \frac{\alpha p^2 \lambda_1}{2} - \frac{\alpha p^2 \lambda_2 \cos\beta}{2} - \frac{(p+\psi_{10})^2 \cos\phi_{10}}{2} - \frac{(p+\psi_{20})^2 \cos\phi_{20}}{2} \right]$$

$$\frac{\partial d}{\partial \tau} = \frac{-\varepsilon}{2p} \left[\zeta pd + \sigma c + \frac{\alpha p^2 \lambda_2 \sin\beta}{2} + \frac{(p+\psi_{10})^2 \sin\phi_{10}}{2} + \frac{(p+\psi_{20})^2 \sin\phi_{20}}{2} \right]$$

$$\frac{\partial \psi_{10}}{\partial \tau} = \varepsilon \left\{ \frac{\mu p^2}{2} \left[(b+c)\cos\phi_{10} + (d-a)\sin\phi_{10} \right] - \mu\zeta_1 \psi_{10} - \mu\zeta_0 (p+\psi_{10})^2 \mathrm{sgn}(\psi_{10}) \right\}$$

$$\frac{\partial \psi_{20}}{\partial \tau} = \varepsilon \left\{ \frac{\mu p^2}{2} \left[(b+c)\cos\phi_{20} + (d-a)\sin\phi_{20} \right] - \mu\zeta_1 \psi_{20} - \mu\zeta_0 (p+\psi_{20})^2 \mathrm{sgn}(\psi_{20}) \right\}$$

$$\frac{d\phi_{10}}{d\tau} = \psi_{10}$$
$$\frac{d\phi_{20}}{d\tau} = \psi_{20} \quad (10)$$

These are a set of eight first-order autonomous differential equations describing the slow dynamics of the system. The steady-state solutions approximated based on Eq. (10) are given in the next section.

4 Steady-state responses

To find the most important steady-state solution for the perfect balancing position and the stability of the system's slow dynamics with an aim of evaluating the performance of the ABB system, we use Eq. (10) to predict the position of the balancing balls.

By equating Eq. (10) to zero and acknowledging that $\psi_{S10} = \psi_{S20} = 0$, i.e., the balls are motionless in a steady state, we find a solution for the perfect balancing position. The solution is discussed in the following sections. This type of solution has different ball positions corresponding to frequencies above and below the natural frequency.

4.1 Perfect balancing solution

The solutions for the motion of suspension are negligible, i.e., $a_S = b_S = c_S = d_S = 0$. The corresponding ball positions can be found easily by solving the following equation numerically.

$$\sin\phi_{S10} + \sin\phi_{S20} = -\alpha\lambda_2 \sin\beta, \cos\phi_{S10} + \cos\phi_{S20} = -\alpha\lambda_1 - \alpha\lambda_2 \cos\beta,$$

On solving, we get Eq. (11)

$$\sin^2(\varphi_{S10}-\varphi_{S20}) = 1-\left[\frac{\alpha^2(\lambda_1^2+\lambda_2^2)}{2}+\alpha^2\lambda_1\lambda_2\cos\beta-1\right]^2 \quad (11)$$

On the basis of the form of Eq. (11), we inferred that a pair of balancing balls sticks together below the natural frequency of suspension and diverges to distinct positions above the natural frequency in a steady state. For this type of solution, as $a_S = b_S = c_S = d_S = 0$, the system exhibits almost no residual vibrations. This is the desired solution to minimize radial vibrations.

We use perturbation methods to make Eq. (10) linear and assume that each solution a, b, c, d, ϕ_{10}, ϕ_{20}, ψ_{10}, and ψ_{20} has small perturbation values Δa, Δb, Δc, Δd, $\Delta\phi_1$, $\Delta\phi_2$, $\Delta\psi_1$, and $\Delta\psi_2$, respectively, in Eq. (12):

$$a = a_S+\Delta a \quad b = b_S+\Delta b \quad c = c_S+\Delta c$$
$$d = d_S+\Delta d \quad \phi_{10} = \phi_{S10}+\Delta\phi_1 \quad \phi_{20} = \phi_{S20}+\Delta\phi_2$$
$$\psi_{10} = \psi_{S10}+\Delta\psi_1 \quad \psi_{20} = \psi_{S20}+\Delta\psi_2 \quad (12)$$

Next, we express matrix A_x as follows:

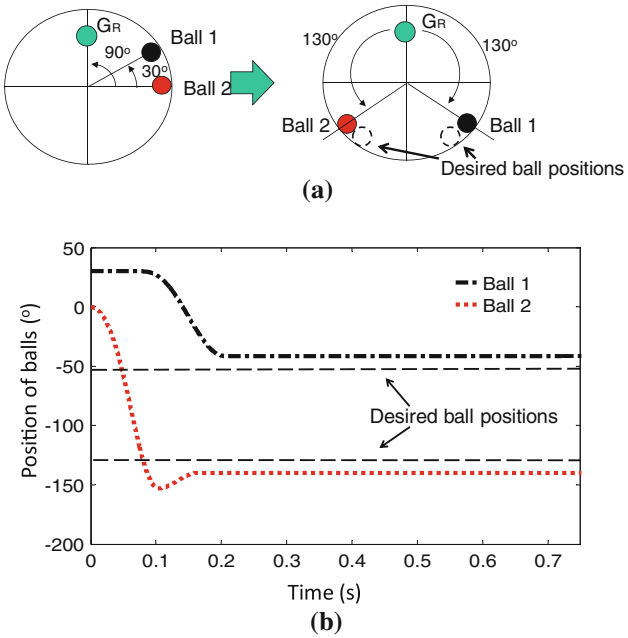

Fig. 3 Variation in position of the balls as $\alpha_0 = 1\times10^{-6}$ m

$$\Delta X(\tau) = [\Delta a\,\Delta b\,\Delta c\,\Delta d\,\Delta\phi_1\,\Delta\phi_2\,\Delta\psi_1\,\Delta\psi_2]^T$$

$$A_x = \begin{bmatrix}
-\frac{\varepsilon\zeta}{2} & \frac{\varepsilon\sigma}{2p} & 0 & 0 & \frac{\varepsilon p}{4}\cos\phi_{S10} & \frac{\varepsilon p}{4}\cos\phi_{S20} & \frac{\varepsilon}{2}\sin\phi_{S10} & \frac{\varepsilon}{2}\sin\phi_{S20}\\
-\frac{\varepsilon\sigma}{2p} & -\frac{\varepsilon\zeta}{2} & 0 & 0 & \frac{\varepsilon p}{4}\sin\phi_{S10} & \frac{\varepsilon p}{4}\sin\phi_{S20} & -\frac{\varepsilon}{2}\cos\phi_{S10} & -\frac{\varepsilon}{2}\cos\phi_{S20}\\
0 & 0 & -\frac{\varepsilon\zeta}{2} & \frac{\varepsilon\sigma}{2p} & \frac{\varepsilon p}{4}\sin\phi_{S10} & \frac{\varepsilon p}{4}\sin\phi_{S20} & -\frac{\varepsilon}{2}\cos\phi_{S10} & -\frac{\varepsilon}{2}\cos\phi_{S20}\\
0 & 0 & -\frac{\varepsilon\sigma}{2p} & -\frac{\varepsilon\zeta}{2} & \frac{-\varepsilon p}{4}\cos\phi_{S10} & \frac{-\varepsilon p}{4}\cos\phi_{S20} & -\frac{\varepsilon}{2}\sin\phi_{S10} & -\frac{\varepsilon}{2}\sin\phi_{S20}\\
0 & 0 & 0 & 0 & 0 & 0 & 1 & 0\\
0 & 0 & 0 & 0 & 0 & 0 & 0 & 1\\
\frac{-\varepsilon\mu p^2}{2}\sin\phi_{S10} & \frac{\varepsilon\mu p^2}{2}\cos\phi_{S10} & \frac{\varepsilon\mu p^2}{2}\cos\phi_{S10} & \frac{\varepsilon\mu p^2}{2}\sin\phi_{S10} & 0 & 0 & (-\varepsilon\mu\varsigma_1-2\varepsilon\mu\varsigma_0 p)/2 & 0\\
\frac{-\varepsilon\mu p^2}{2}\sin\phi_{S20} & \frac{\varepsilon\mu p^2}{2}\cos\phi_{S20} & \frac{\varepsilon\mu p^2}{2}\cos\phi_{S20} & \frac{\varepsilon\mu p^2}{2}\sin\phi_{S20} & 0 & 0 & 0 & (-\varepsilon\mu\varsigma_1-2\varepsilon\mu\varsigma_0 p)/2
\end{bmatrix}$$

If $\Delta\underline{X}(\tau) = e^{s\tau}$, then $[A_x - \underline{I}\,S]\Delta\underline{X}(\tau) = 0$, where S is an eigenvalue, $[A_x - \underline{I}S] = 0$ is the perturbation characteristic equation, and I is the unit matrix. Hence, from this solution, we obtain eigenvalues of the system and can estimate its stability. If all the eigenvalue has real parts that are less than zero, the system is stable, otherwise, the system is unstable.

5 Time response and stability analysis

Figure 3a shows the position of a pair of balls at initial angles 0° and 30°. At 130°, the balls are positioned at $|\beta-\phi_1|$ and $|\beta-\phi_2|$ (see Fig. 3b) because of the inherent imbalance in the ABB.

With the obtained solutions, a stability analysis is performed to determine the stability of each steady-state solution. Design guidelines are assured for achieving the desired performance by the ABB system. The analysis is carried out using stability diagrams constructed with respect to variations in the main design parameters, operating speed ratio ($p = \omega/\omega_n$) and scaling parameter ($\varepsilon = \sqrt{m/M}$). Figure 4 shows the stability diagram for the perfect balancing solution. This solution renders the best radial vibration reduction among all solutions. To ensure the stability of this perfect balancing solution, we need to design an ABB system such that (p,ε) falls in the square region in Fig. 4.

To obtain such a design, three conditions related to the system parameters must be satisfied. First, the system has to operate above the resonance frequency, i.e., $p > 1.3$. Second, the maximal counterbalance (two balls sticking together) has to be greater than the inherent imbalance, i.e., $2mR > M_R e$, which corresponds to the area $\varepsilon \geq 0.03$ in Fig. 4. Third, the total mass of the balls has to be sufficiently small for ε to not exceed a certain level to avoid degradation of the stability of the ABB system, which corresponds to the curve representing the upper boundary of the square region in Fig. 4.

Next, we present some numerical simulation results. Figure 5 shows the computed ranges of the desired perfect balancing solution with respect to the rotor speeds of $p = 6$ for $\varepsilon = 0.18$, $\varepsilon = 0.15$, and $\varepsilon = 0.1$, respectively. When the lead angle for imbalance in the mass of the balancing balls is $\beta = 180°$, the ranges of the angular displacement of the ball positions are symmetrical. These design parameters can automatically satisfy the balance requirement when α_0 approaches 0 m. However, the mass of the balancing balls can almost completely eliminate radial vibrations via the concept of counterbalancing. We find that the angular displacement of the ball positions varies in a wide range when α_0 approaches 2×10^{-6} m, as shown in Fig. 5. However, p and ε are the other main system parameters that can affect the angular displacement of the ball positions within a wide range. The results of the numerical simulation are shown in Fig. 5. From this result, an overlap region can be seen with an increase in the rolling friction.

The lead angle is opposite to the balancing balls. The angle of two balancing balls, which is in $\varepsilon = 0.1$, is getting closer than it in $\varepsilon = 0.15$ and $\varepsilon = 0.18$, respectively as shown in Fig. 5. From Fig. 6, it is observed that when $p = 3$ and $p = 6$, the desired ranges change at the same time. However,

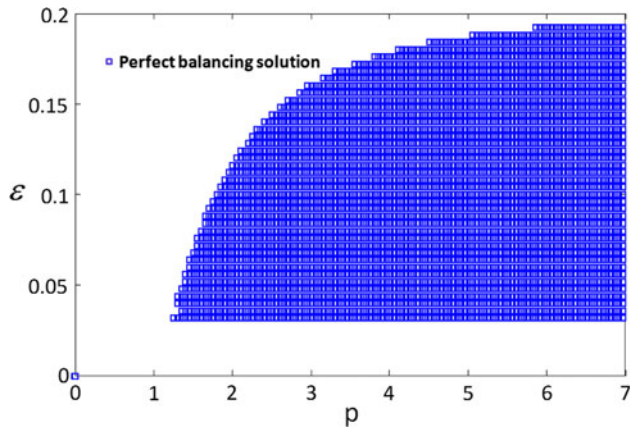

Fig. 4 Stability diagram of scaling parameter ε versus speed ratio p for the perfect balancing solution

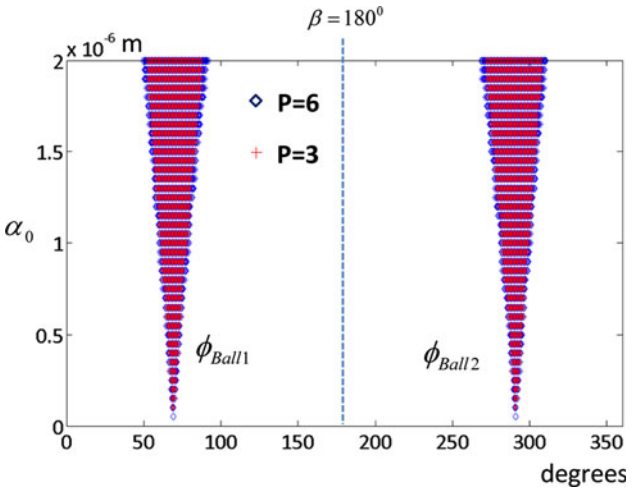

Fig. 6 Range of angular displacements of ball positions for perfect balancing solution with $p = 3$ and $p = 6$

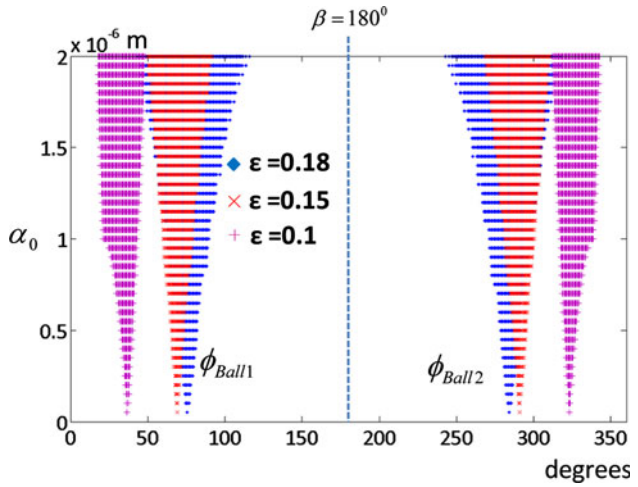

Fig. 5 Ranges of angular displacement of the balls' position for the perfect balancing solution with ε

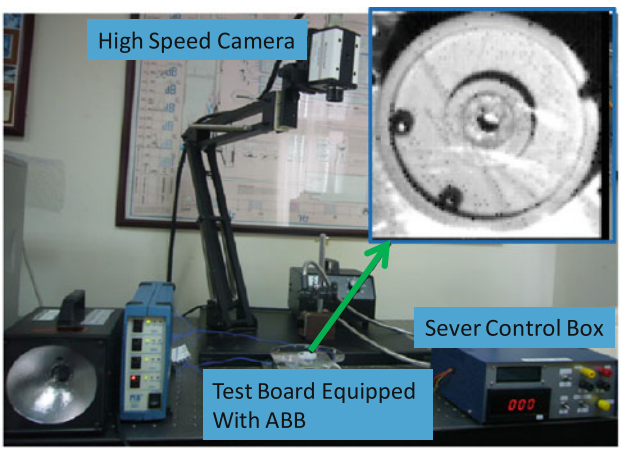

Fig. 7 Photograph of experimental setup for measuring positions of the balls

we find that p can affect the desired angular range. We find that when $p = 3$, the ranges of the angular displacement of the balls' position becomes narrower than that when $p = 6$. Therefore, the ranges of angular displacement of the balls' position at $p = 6$ and $p = 3$ can overlap as shown in Fig. 6.

6 Experimental study

The performance of the ABB is characterized by the residual vibration of the rotor system, which is caused by the failure of the balls' position to counterbalance the mass imbalance. In this study, we used an optical disk drive system with a high-speed camera to verify the results obtained by the computer simulations along with software to record the balls' positions. The photograph of the experimental setup for measuring the positions of the balls is shown in Fig. 7.

The circular races were made from Si_3N_4. The Si_3N_4 balls and races were required to be sufficiently smooth to ensure that the rolling friction was greatly reduced. Figure 8a shows the comparison of the experimental results

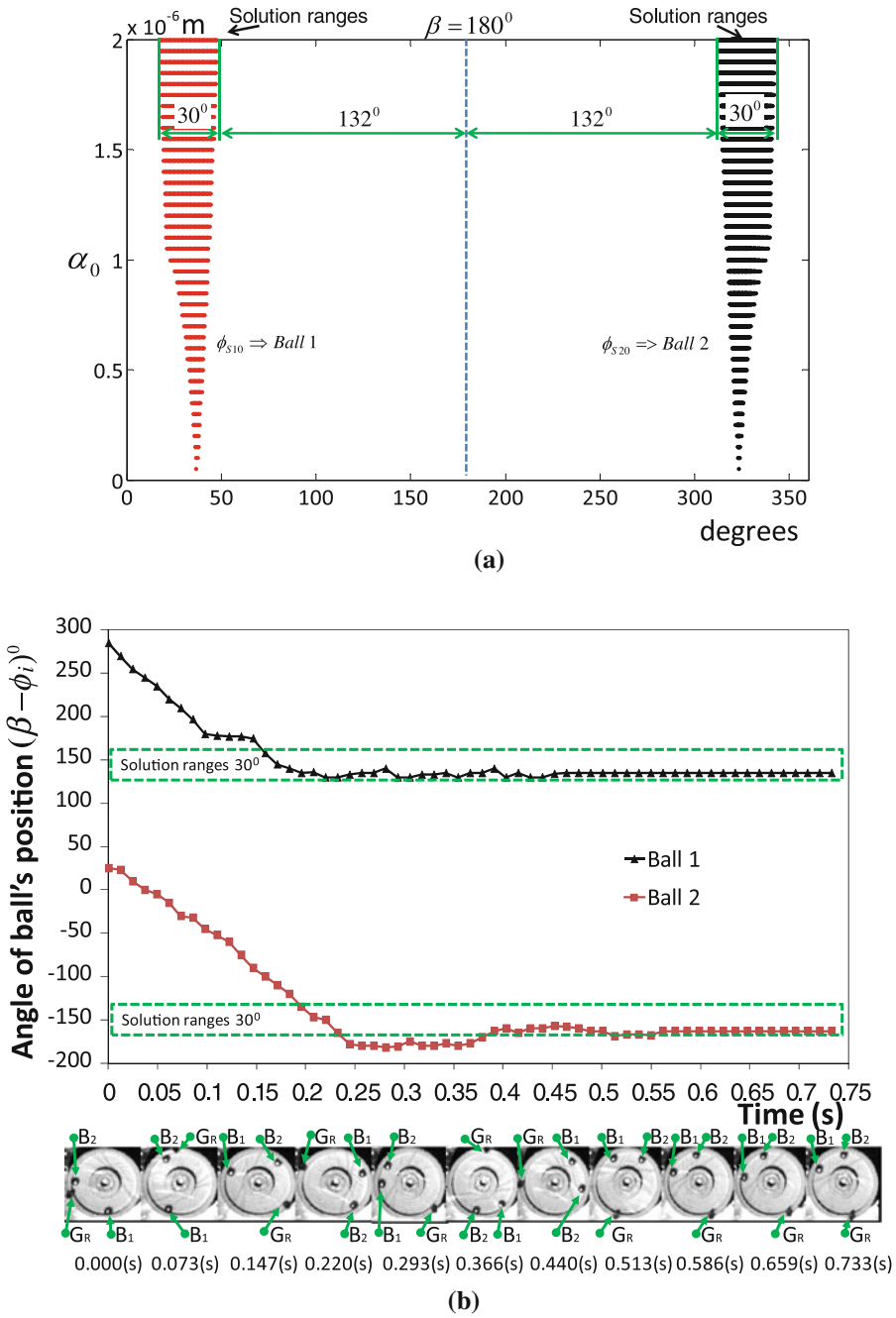

Fig. 8 **a** Range of the balls' positions for the perfect balancing solution with $p = 4.47$; **b** experimental results of the balls' positions

with the simulation results, with $p = 4.47$ and the rolling friction was 2×10^{-6} m. We found that the range for the two balancing balls was 30° when the rolling friction was 2×10^{-6} m. The inherent imbalance of the rotor system was identified prior to the experiments. To record the balls' positions corresponding to mass imbalance using the software, reference points were used to denote the unbalanced mass (G_R). The experiment was carried out as follows. The motor was powered by a power supply through the control box to accelerate the rotational speeds of the rotor to the desired speeds. We used a high-speed camera to observe G_R with respect to the angular displacements of the two balancing balls from the transient state to the steady state, as shown in Fig. 8b. The final rotor speed is approximately 3,000 rpm ($p = 4.47$). The balancing balls are observed to be positioning at the boundary of the solution ranges.

From these results, we find the position of the balancing balls to be at the boundary of the solution ranges, when the rotor rotational speeds are above the first natural frequency. We verified that the angular displacement of the positions of the balls is the key factor affecting the ABB performance. In this research, it was important to monitor and record the angular displacement of the balancing balls' positions related to the unbalanced mass from its static state up to the desired speed. The experimental results verified the validity of the established mathematical model, which in turn confirmed the analytical results.

7 Conclusions

This study investigated the effects of the rolling friction, speed ratio, and scaling parameter on the position of the balls in an ABB to obtain a perfect balancing position. The rolling friction of the balls against the racer was found to be the main reason for residual vibrations. The ABB can be designed using the mathematical model parameters in the stable regions. The range of the angular displacement of the balls' position in the perfect balancing solution is also affected by factors such as the speed ratio and scaling parameter. The constructed experimental apparatus was successfully used to verify the mathematical model.

Acknowledgments The authors are greatly indebted to the National Science Council of the R.O.C. for supporting the research through contracts (grant numbers NSC-96-2221-E-007-075, and NSC-97-2221-E-007- 050-MY3).

References

Chan TC, Sung CK, Chao CP (2011) Non-linear suspension of an automatic ball balancer. Int J Non-Linear Mech 46:415–424

Chao CP, Sung CK, Leu HC (2005) Effects of rolling friction of the balancing balls on the automatic balancer for optical disk drives. J Tribol Trans ASME 127(4):845–856

Chao CP, Sung CK, Wu ST, Huang JS (2007) Non-planar modelling and experimental validation of a spindle—disk system equipped with an automatic balancer system in optical disk drives. Microsyst Technol 13(8–10):1227–1239

Cheng CC, Wu FT, Hsu KS, Ho KL (2008) Design and analysis of auto-balancer of an optical disk drive using speed-dependent vibration absorbers. J Sound Vib 311:200–211

DeSmidt HA (2009) Imbalance vibration suppression of a supercritical shaft via an automatic balancing device. J Vib Acoust Trans ASME 131(4):1–13

Lim S, Kim K, Cho U, Park NC, Park YP, Park KS, Lee HB, Yoo SH (2011) Flexible auto balancer design for the reduction of optical disk drive vibration. Microsyst Technol 17:945–951

Liu J, Ishida Y (2009) Vibration suppression of rotating machinery utilizing an automatic ball balancer and discontinuous spring characteristics. J Vib Acoust Trans ASME 131(4):1–7

Lu CJ, Wang MC, Huang SH (2008) Analytical study of the stability of a two-ball automatic balancer. Mech Syst Signal Process 23(3):884–896

Quangang Y, Ong EH, Sun J, Guo G, Lim SP (2004) Study on the influence of friction in an automatic ball balancing system. J Sound Vib 285:73–99

Rajalingham C, Bhat RB (2006) Complete balancing of a disk mounted on a vertical cantilever shaft using a two ball automatic balancer. J Sound Vib 290:169–191

Rodrigues DJ, Champneys AR, Friswell MI, Wilson RE (2011) Experimental investigation of a single-plane automatic balancing mechanism for a rigid rotor. J Sound Vib 330:385–403

Van De Wouw N, Van Den Heuvel MN, Nijmeijer H, Van Rooij JA (2005) Performance of an automatic ball balancer with dry friction. Int J Bifurc Chaos 15(1):65–82